Nanoscale

PAPER

View Article Online
View Journal | View Issue

Cite this: *Nanoscale*, 2024, **16**, 21351

Engineering circularly polarized light emission in nanostructured oligodimethylsiloxane-helicene chiral materials†

Stefano Cadeddu,[a] Bart W. L. van den Bersselaar,[b] Bas de Waal,[b] Marie Cordier,[a] Nicolas Vanthuyne,[c] Stefan C. J. Meskers,*[b] Ghislaine Vantomme*[b] and Jeanne Crassous*[a]

Chiroptical properties in the bulk state can be tuned by controlling the formation of chiral ordered nanostructures. Here, we present a series of discrete oligodimethylsiloxane-helicene-pyrene block molecules with varying *o*DMS lengths and study the nanostructures formed in both bulk and solution, including their chiroptical properties. In bulk, ordered 2D nanostructures self-assemble, driven by phase segregation induced by the siloxane oligomers, with clear differences in the properties of the racemic and enantiopure versions. Moreover, intermolecular pyrene interactions lead to excimer emission. As a result, up to a 5-fold increase in circularly polarized luminescence is observed in the solid state as compared to the solution, accompanied by a clear influence of the pyrene excimer emission on the overall emission process. Interestingly, in the ordered lamellar packing achieved from long *o*DMS units, the excimer emission shows very little net circular polarization, while in the disordered state achieved from shorter *o*DMS units, this excimer emission displays a significant degree of circular polarization. These results demonstrate that functionalizing chiroptical building blocks with discrete oligodimethylsiloxane chains is a versatile strategy to control photophysical properties and modulate chiroptical emission in bulk. This approach advances the integration of chiroptical materials into devices, enabling diverse applications ranging from optoelectronics to communication technologies.

Received 18th August 2024,
Accepted 14th October 2024

DOI: 10.1039/d4nr03389b

rsc.li/nanoscale

Introduction

Helicenes are helical semiconducting molecules formed from *ortho*-fused aromatic rings that exhibit attractive properties such as strong chiroptical activity (intense electronic circular dichroism – ECD, and circularly polarized luminescence – CPL). Helicenes therefore hold great promise for applications in diverse domains such as optoelectronics, spintronics and bioimaging.[1] While their photophysical and chiroptical properties have been well studied and examined in solution, studies in the condensed phase, as in ordered gels, mesophases or the solid state, remain scarce. Indeed, the assembly of helicene derivatives is particularly challenging as it requires a rational design to balance the complementary recognition units connecting the helicene monomers into an ordered structure and the compatibility between the various peripheral functional groups.[2] For instance, the formation of fibers through columnar organization has been reported by Katz and coworkers for a carbo[6]helicene bearing terminal *para*-quinones and four dodecyloxy chains.[2a,b] These supramolecular stacks result in gigantic optical rotation values, strong circular dichroic responses and linearly/circularly polarized emission. Similarly, supramolecular trimeric aggregates displaying a fibrous structure with improved CPL responses compared to monomeric phthalhydrazide helical units have been described by Takeuchi and coworkers.[2c] Following a self-assembly strategy developed by Sánchez and coworkers on carbo[5]helicenes,[2e] our group has recently evidenced a CPL inversion effect upon self-assembly of carbo[6]helicenes decorated with bisamide units.[2f] In addition, the group of Yamaguchi has thoroughly examined the self-assembly processes of 1,14-dimethyl-tetrahelicenic oligomers (see ref. 2*h* and references therein). These reports highlight the ongoing progress in the field and serve as inspiration for the development of new

[a]*Institut des Sciences Chimiques de Rennes, Univ Rennes, UMR CNRS 6226, Campus de Beaulieu, 35042 Rennes Cedex, France. E-mail: jeanne.crassous@univ-rennes.fr*
[b]*Institute for Complex Molecular Systems and Laboratory of Macromolecular and Organic Chemistry, Department of Chemical Engineering and Chemistry, Eindhoven University of Technology, P.O. Box 513, 5600 MB Eindhoven, The Netherlands. E-mail: s.c.j.meskers@tue.nl, g.vantomme@tue.nl*
[c]*Aix Marseille Univ, CNRS, Centrale Med, FSCM, Marseille, France*

†Electronic supplementary information (ESI) available. CCDC 2368946 and 2368947. For ESI and crystallographic data in CIF or other electronic format see DOI: https://doi.org/10.1039/d4nr03389b

methods to control photophysical properties in bulk, to integrate helicene materials into devices, as well as to understand the mechanisms at play.[3]

Recently, the functionalization of crystalline moieties with discrete oligodimethylsiloxanes (*o*DMS) has emerged as a versatile strategy to achieve long-range order with sub-5 nm domain spacings.[4] These block co-oligomers (BCOs) or block molecules consist of a "hard" molecular core and a "soft" amorphous *o*DMS chain that induce phase separation into different morphologies.[5] In such systems, synergistic effects between directional interactions and phase separation promote the assembly of complex nanostructures in a highly controlled manner with unique properties. For example, *o*DMS chains have been functionalized with azobenzenes resulting in photo-switchable nanomaterials,[5a] dinitrophenylhydrazones for the construction of highly ordered thermosensitive nanomaterials,[5b] as well as diphenylanthracenes for the emission of upconverted, linearly polarized light.[5c]

Inspired by this work, we intended to combine carbo[6]helicene as a π-conjugated helical core with *o*DMS side chains and generate self-assembled ordered nanostructures. We hypothesized that the amorphous liquid-like siloxane matrix should influence the chiroptical response of helicenes. Herein, we report the synthesis of *o*DMS end-functionalized carbo[6]helicenes and their resulting physicochemical and morphological properties in bulk. A series of enantiopure *P*- and *M*-carbo[6]helicenes coupled with siloxane oligomers of different chain lengths at both the 4- and 13-positions were synthesized (**Hel-Si$_3$**, **Hel-Si$_7$** and **Hel-Si$_{11}$** in Fig. 1) and their photophysical and chiroptical properties were studied, both in solution and in bulk. This was performed with the aim of achieving optimized CPL activity through lamellar morphology. The helical core was decorated with pyrene units at its 2,15-positions and the typical pyrene-based monomeric/excimeric emission response was analysed. The formation of 2D layered bulk assemblies was characterized in solution and in the solid state by (chir) optical spectroscopy (UV/Vis, ECD, emission and CPL), polarized optical microscopy (POM), differential scanning calorimetry (DSC), and medium/wide-angle X-ray scattering (MAXS/WAXS) to identify the formed nanostructures and to elucidate the molecular features leading to the emerging macroscopic photophysical and chiroptical properties. Pleasingly, up to a 5-fold increase in CPL activity was observed in the lamellar ordered phase as compared to the solution, accompanied by a clear influence of the pyrene excimer emission on the overall emission process.

Results and discussion

Design and synthesis of oligodimethylsiloxane-helicenes

The synthesis of enantiopure *P*-carbo[6]helicene derivatives **Hel-Si$_3$**, **Hel-Si$_7$** and **Hel-Si$_{11}$** as helical BCOs is depicted in Scheme 1. The same procedure is followed for the *M*-derivative. First, enantiopure *P*- and *M*-7 derivatives were prepared, bearing two bromides and two pent-1-enyl-oxy groups at the 2,15- and 4,13-positions, respectively (see the ESI† for detailed procedures). A classical Wittig reaction between (2,7-naphthalenedimethylene)-bis[triphenylphosphonium bromide] **1**[6] and 4-bromo-2-methoxy-benzaldehyde **2** was followed by an oxidative photocyclization (Mallory reaction)[7] to yield 2,15-dibromo-4,13-dimethoxy-carbo[6]helicene **4**, as a novel helicene derivative which was subsequently resolved into its pure enantiomers by using HPLC separations over a chiral stationary phase (see conditions in the ESI†). Demethylation using BBr_3 yielded *P*- and *M*-2,15-dibromo-4,13-dimethoxy-carbo[6]helicene **5**. Since **5** appeared to be unstable, it was thus directly engaged in a nucleophilic substitution using bromopent-1-ene. The obtained enantiopure helical derivatives *P*- and *M*-7, bearing two terminal olefins, were ready to react with siloxanes of different lengths through a hydrosilylation reaction using Karstedt's catalyst. The helicenes were coupled with three different lengths of *o*DMS chains, respectively, with 3, 7 and 11 silicon atoms yielding *P*- and *M*-**Hel-Br-Si$_3$**, **Hel-Br-Si$_7$**, and **Hel-Br-Si$_{11}$** in 59–73% yields. Finally, a classical Suzuki coupling with pyrene-2-boronic acid gave access to enantiopure helical compounds *P*- and *M*-**Hel-Si$_3$**, **Hel-Si$_7$**, and **Hel-Si$_{11}$** as waxy solids (Fig. 1 and Scheme 1), which were fully characterized by NMR spectroscopy and mass spectrometry (see Fig. S1–S38†).

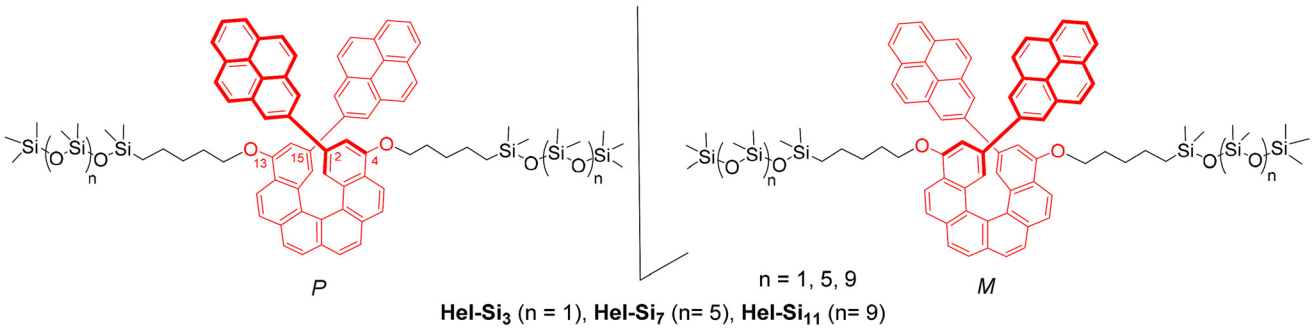

Fig. 1 Chemical structures of the carbo[6]helicene derivatives studied, bearing 2-pyrenyl chromophores at its 2,15-positions and two *o*DMS chains of diverse lengths at the 4,13-positions.

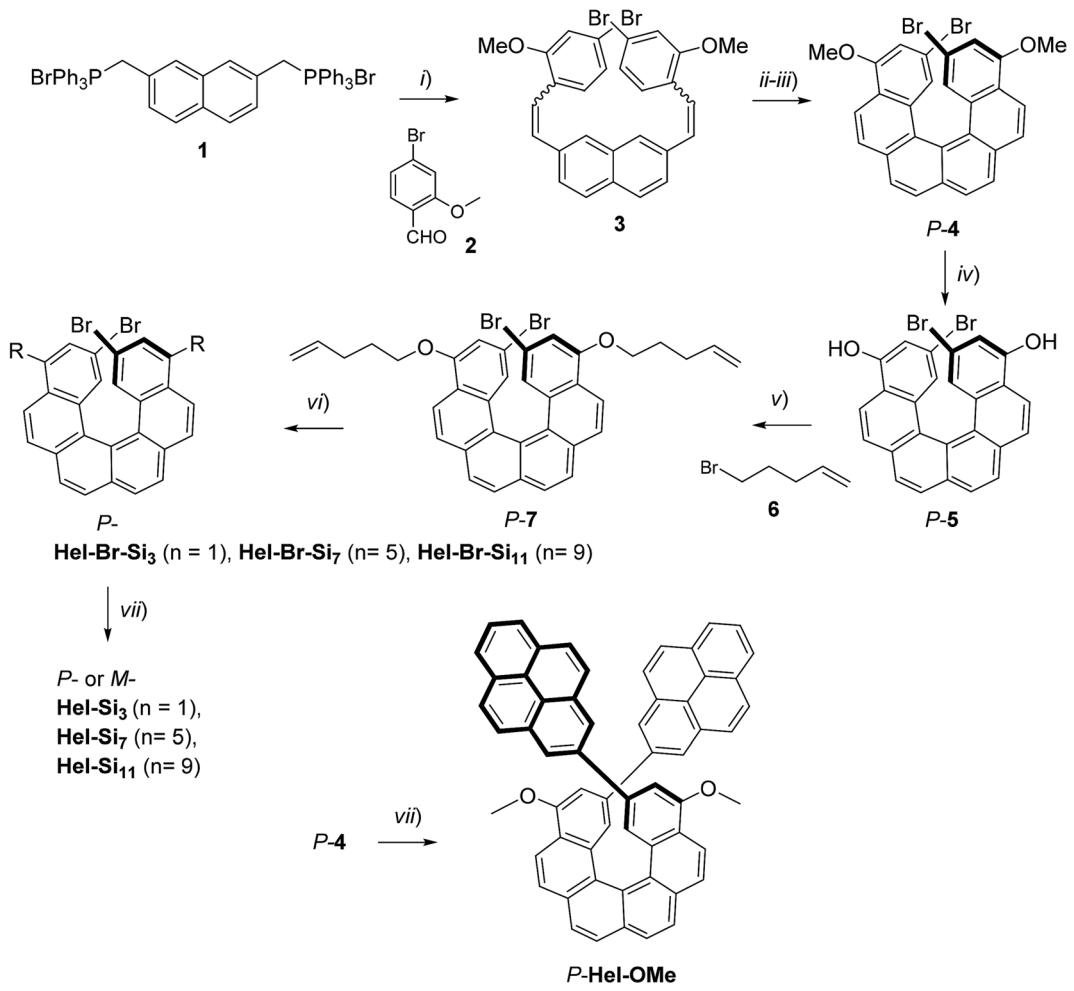

Scheme 1 Synthetic route to enantiopure *o*DMS end-functionalized carbo[6]helicenes *P*-**Hel-Si**$_{3,7,11}$ and **Hel-OMe**. (i) *n*-BuLi, rt, Ar, 3 h, 94%; (ii) I_2, toluene, Ar, propylene oxide, $h\nu$, 7 h, 61%; (iii) chiral HPLC resolution (see the ESI†); (iv) BBr_3, CH_2Cl_2, rt, Ar, 12 h; (v) K_2CO_3, DMF, Ar, 65 °C, overnight, 67%; (vi) Karstedt's catalyst, $\mathbf{Si_{(2+n)}H}$, CH_2Cl_2, rt, Ar, 12 h, 73% (n = 1), 59% (n = 5, 9); (vii) pyrene-2-boronic acid, $Pd(PPh_3)_4$, Na_2CO_3, DMF, 80 °C, Ar, 12 h, 43–55%. The same strategy was used for the *M* enantiomers. The detailed R substituents can be seen in Fig. 1.

UV-vis absorption and ECD responses of Hel-Si$_n$ in solution and the solid state

UV-vis and ECD spectroscopies are dependent on the absolute configuration of a molecule and on its overall conformation, making them powerful tools for analysing aggregation in solution. The UV-vis absorption responses of **Hel-Si$_n$** in methylcyclohexane (MCH) solutions are shown in Fig. 2a–c. All enantiomers show identical UV and mirrored ECD spectra, as expected for enantiomerically pure compounds. Under these conditions, the three systems clearly show very similar responses, with strong absorption bands at 240, 280, 325, 345 and 375 nm, and ε values up to 7×10^4 M^{-1} cm^{-1}. As anticipated, all the absorption bands are strongly ECD active (see Fig. 2a–c, upper curves). For instance, the *P*-**Hel-Si$_3$** enantiomer exhibits respective $\Delta\varepsilon$ values of −206, −130, −57, −82 and +250 M^{-1} cm^{-1}, when going from higher to lower energies. Due to their strong similarities, we conclude that the ECD response originates from the helical backbone without the *o*DMS units, since they are similar to those measured in CH_2Cl_2 and to the **Hel-OMe** enantiomers (Fig. S43–S55†), thus confirming the absence of assembly at 10^{-5} M concentrations in MCH. It should be noted that all the samples were also analysed in solvent/antisolvent THF/MCH mixtures to induce the aggregation in solution (Fig. S56–S61†). No significant changes in the ECD spectra were observed, indicating that the optical properties in the ground state do not reflect an aggregation process in solution. This observation also indicates that the emission in solution comes from the molecularly dissolved state (*vide infra*).

The molecules also exhibit interesting chiroptical properties in the solid state (Fig. 2d–f). Solid-state samples were prepared by drop casting onto quartz substrates, and the films were then annealed (see the ESI† for more details). In the solid state, the enantiomers show different UV spectra and non-perfectly mirrored ECD spectra. These differences are rationalized to be due to sample preparation, which tends to create inhomogeneities in the thickness and arrangement of the samples.

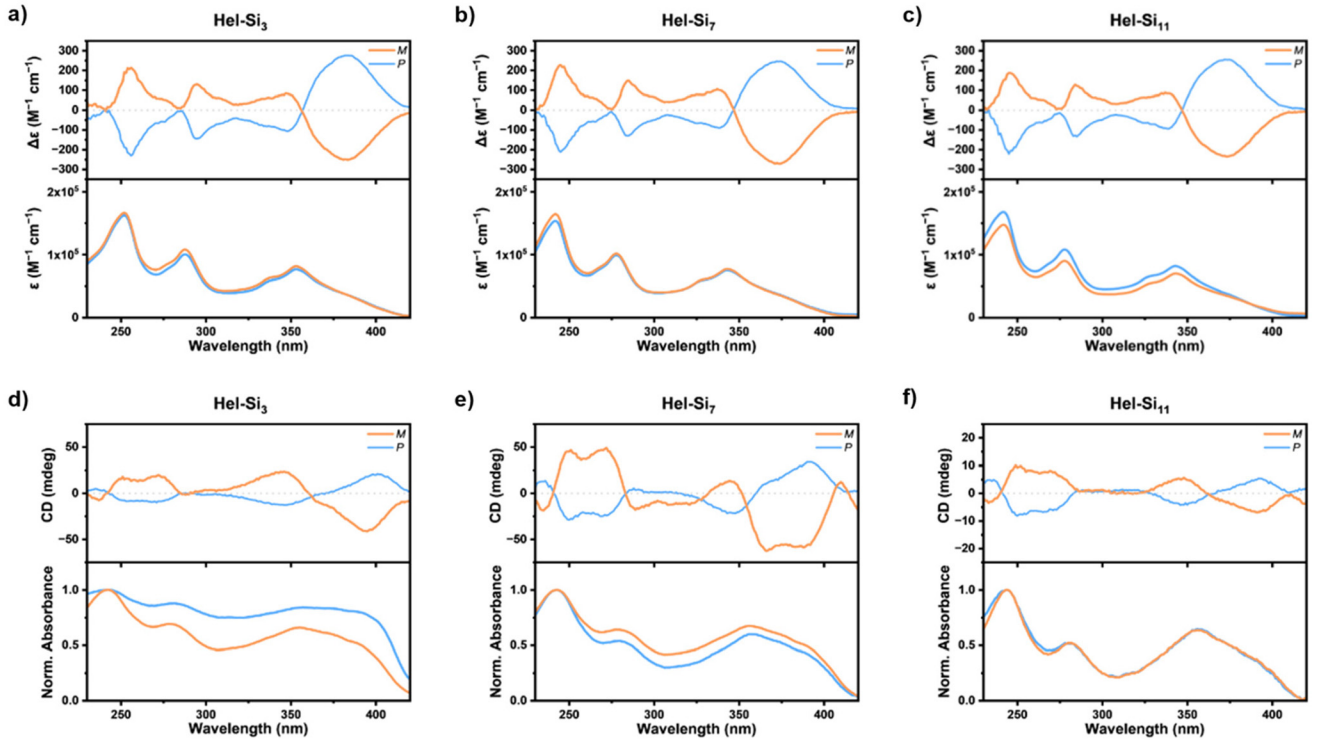

Fig. 2 (a–c) Comparison of UV-vis absorption and ECD responses of **Hel-Si$_n$** in MCH solutions ($C \sim 1–2 \times 10^{-5}$ M) and (d–f) in the solid state (solutions dropcast onto quartz substrates and annealed).

Indeed, due to the low quantities of material available, it was difficult to adjust the film thickness for obtaining the mirror-image relationship. In addition, the UV-vis and ECD responses differed from those previously observed in solution. While at higher energies (*i.e.* between 200 and 330 nm) the UV-vis responses were similar with the presence of two bands, and the bands above 350 nm were found to be broader, with higher intensities around 400 nm and with an onset starting around 430 nm, thus highlighting a bathochromic shift of these low-energy bands when going from solution to the solid state. Interestingly, one can notice that there is a systematic extinction of the ECD bands corresponding to the absorption around 280 nm. This phenomenon is most probably related to the supramolecular alignment of the helical species, as already highlighted by Wade *et al.* in helicene systems well-oriented on surfaces.[8] It should be noted that although only slight anisotropy effects were observed when the samples were rotated or the back and front surfaces were switched (see Fig. S59–S65†), the averaged ECD spectra were still considered.

Nanostructures of Hel-Si$_n$ in bulk

To elucidate the thermal stability of **Hel-Si$_n$**, the materials were analysed by DSC (Fig. S39,† Table 1). Functionalization of the helicenes with a discrete *o*DMS chain resulted in a reversible transition at elevated temperatures. **Hel-Si$_3$** showed this transition at the highest temperature (T_m = 187–196 °C), which was expected since the volume fraction of the crystalline unit is highest in this material. Moreover, both enantiomers as well as the racemic mixture of **Hel-Si$_3$** showed cold crystallization between 108–116 °C. Enantiomerically pure **Hel-Si$_7$** and **Hel-Si$_{11}$** exhibited regular crystallization and melting transitions, with temperatures decreasing almost linearly with increasing siloxane content. Besides, similar to the solid-state UV-vis and ECD data (Fig. 2d–f), the *M*- and *P*-**Hel-Si$_n$** enantiomers show differences in T_m, T_c, and ΔH_{fus} due to sample inhomogeneity. Strikingly, the racemic mixtures of **Hel-Si$_7$** and **Hel-Si$_{11}$** exhibited lower T_c and these exothermic transitions were observed only upon heating. We hypothesize that this effect originates from slower crystallization in the racemic mixture compared to

Table 1 Bulk characterization of **Hel-Si$_n$**

Name	Enantiomer	T_m [°C]	T_c [°C]	ΔH_{fus} [kJ mol^{-1}]	Phase[a]	d[a] [nm]
Hel-Si$_3$	*M*	196	108[b]	11.8	DIS	—
	P	186	115[b]	7.0	DIS	—
	Racemate	188	116[b]	27.8	LAM	2.4
Hel-Si$_7$	*M*	151	136	10.4	LAM	4.1
	P	145	125	8.3	LAM	4.1
	Racemate	108	76[b]	9.4	LAM	3.8
Hel-Si$_{11}$	*M*	116	90	10.3	LAM	5.3
	P	114	88	8.7	LAM	5.3
	Racemate	110	49[b]	35.6	LAM	4.6

[a] Morphology of the nanostructure determined with MAXS/WAXS at room temperature. DIS = disordered, LAM = lamellar phase. Domain spacing (d) was calculated using $d = 2\pi/q$. [b] Observed as cold crystallization.

the enantiomerically pure substrates. In these racemic mixtures, we also observed a decreasing T_c with increasing siloxane content, similar to the enantiomerically pure materials. This trend indicates that the *o*DMS side chains have a large influence on the thermal stability of the crystalline phase of **Hel-Si$_n$**. The presence of an ordered structure below T_m was confirmed by the observation of birefringent structures in all enantiomerically pure **Hel-Si$_n$** under the POM (Fig. S40 and S41†). In this part, we thus emphasize the fact that these 2D ordered structures follow the typical racemate properties observed in the crystalline bulk solid state,[9] highlighting a clear difference in behaviour and organization between racemic and enantiopure mixtures. Such different organization is usually not studied in chiral siloxane-based systems[10] although it has direct implications for the material's properties such as semi-conducting properties and charge carrier mobility.[11]

The origin of the phase-separated structures was then investigated using MAXS/WAXS (Fig. 3). Pure enantiomers of **Hel-Si$_3$** showed a primary scattering peak at 2.3 nm^{-1}, but no subsequent scattering peaks were present, indicating the absence of long-range order. In contrast, in the racemate *rac*-**Hel-Si$_3$**, we observed several scattering peaks positioned at integers from the primary peak, indicating a lamellar morphology (q, $2q$, $3q$, ...). Moreover, a low-intensity reflection was positioned at $\frac{1}{2}q$ (q'). We attribute this to a packing defect, similar to those previously reported in the literature.[5a] The resolved lamellar structure has a domain spacing of 2.4 nm. In contrast to the pure enantiomers of **Hel-Si$_3$** and similar to *rac*-**Hel-Si$_3$**, **Hel-Si$_7$** and **Hel-Si$_{11}$** displayed lamellar morphologies in the racemic and enantiopure forms. For *P*- and *M*-**Hel-Si$_7$**, the lamellar morphology was observed with a domain spacing of 4.1 nm. Assuming the side chains are fully stretched, the calculated theoretical length of **Hel-Si$_7$** was approximately 4.0 nm, suggesting that the side chains are indeed present in a stretched conformation. In *rac*-**Hel-Si$_7$**, however, we found the lamellar spacing to be slightly smaller (3.8 nm), indicating partial intercalation of the siloxane side chains. We rationalize that this less efficient packing is also the cause of the slower crystallization observed in the DSC experiments. Moreover, in *P*- and *M*-**Hel-Si$_{11}$** the d_{lam} increased by 1.2 nm compared to *P*- and *M*-**Hel-Si$_7$** to reach 5.3 nm, which is in good agreement with the length of four additional *o*DMS units on both side chains. Hence, we conclude that the phase-separated structures that are formed by *P*- and *M*-**Hel-Si$_7$** and *P*- and *M*-**Hel-Si$_{11}$** consist of stretched molecules. For *M*-**Hel-Si$_7$**, a reflection at q' was observed, similar to that previously described for *rac*-**Hel-Si$_3$**. Moreover, the intensity of the peaks for *P*-**HelSi$_7$** is limited compared to the other spectra of **Hel-Si$_7$**. Due to the waxy nature of this material and the limited amount available, its spectrum was recorded as a thin film on Kapton tape. A more zoomed-in version of the spectrum is shown in Fig. S42.† Interestingly, each **Hel-Si$_n$** showed a distinct peak at 15.6 nm^{-1}, indicated with *, corresponding to a distance of 0.4 nm. We rationalize that this peak originates from the intermolecular distance in the helicene, since it is persistent in all materials. Indeed, the distance between the benzene rings in a [6]helicene has been previously reported to be about 0.4 nm.[12]

To further confirm the validity of our strategy to efficiently and systematically generate lamellar structures in *o*DMS-helicene BCOs, we synthesized **Hel′-Si$_3$** bearing cyanophenyl moieties at the 2,15-positions, which crystallizes readily and provides new insights into the molecular packing (see the ESI†). The X-ray crystallographic structure of **Hel′-Si$_3$** has been resolved (*C*2/*c* centrosymmetric space group) and shows that order is present along both the *b*- and *c*-axes, indicating a tendency to assemble into 2D layered materials (Fig. 4). The widths of both the helicene layers and the *o*DMS layers were found to be 12 Å, which together corresponds well to the lamellar dimension of *rac*-**Hel-Si$_3$** (2.4 nm, *vide supra*). It should be noted that in **Hel′-Si$_3$** no clear π–π stacking is observed because the centroid–centroid distance of 6.4 Å between the intermolecular *p*-CN-phenyl rings is large, and the silicon atoms in the siloxane chains adopt a classical tetrahedral geometry, while the pentyl chains are in a linear zigzag manner, resulting in overall elongated chains. The reported helicity (dihedral angle between the terminal rings of 47.3°)

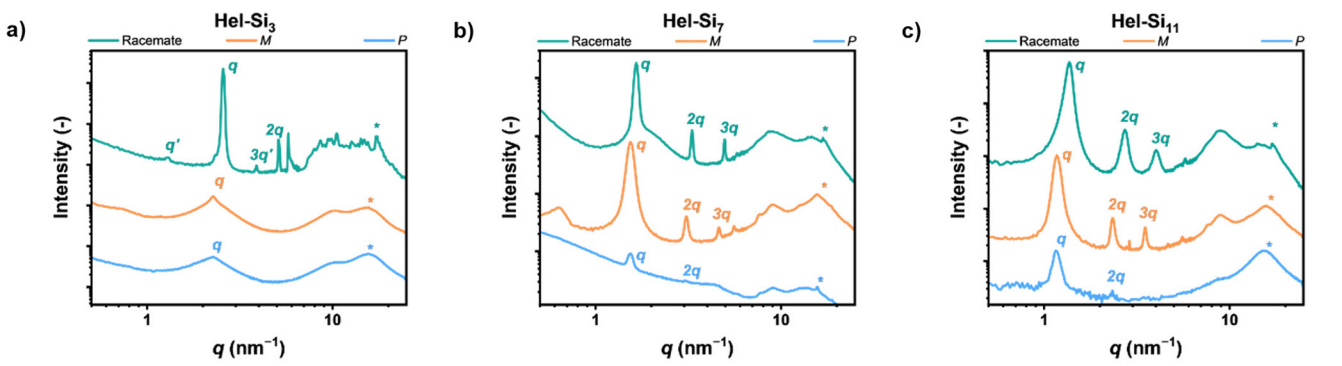

Fig. 3 MAXS/WAXS spectra of the *rac*-, *P*-, and *M*-forms of **Hel-Si$_3$** (a), **Hel-Si$_7$** (b) and **Hel-Si$_{11}$** (c). It should be noted that the curves of *P*-**Hel-Si$_n$** are recorded on Kapton tape due to the small amount synthesized and therefore differences with the enantiomer *M*-**Hel-Si$_n$** are observed due to the different processing conditions and the lower sensitivity of the measurement.

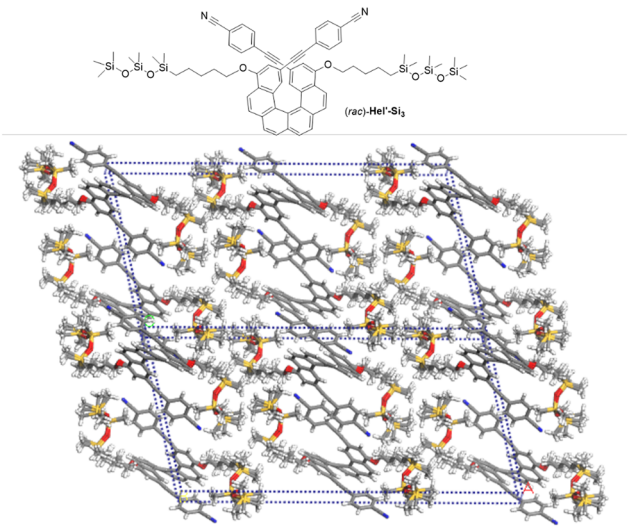

Fig. 4 Chemical structure and supramolecular assembly of 2,15-bis-cyanophenyl-carbo[6]helicene-siloxane adduct *rac*-**Hel'-Si$_3$** obtained from X-ray data analysis.

was in agreement with previously reported values for carbo[6]helicene.[1] For comparison, single crystals of *rac*-**4** were grown and the X-ray analysis revealed that in the absence of siloxane chains, a columnar alignment along the *c*-axis is observed between heterochiral species (*Pbcn* centrosymmetric space group), with π–π stacking between the terminal rings (centroid–centroid distances of 3.9 Å, see Fig. S43 and S44†), confirming that substitution with siloxane chains leads to the formation of a 2D lamellar morphology.

Consequences of self-assembly on the emissive properties of Hel-Si$_n$ in solution and the solid state

The emissive properties of **Hel-Si$_n$** in bulk were then studied to compare with the emissive properties in dilute solution and to understand the role of excimers in the observations. Overall, each **Hel-Si$_n$** shows a similar trend in the solid state and in solution, with deep blue emission in solution and light blue emission in the solid state (Fig. 5, Fig. S70†). The spectrum in solution has the typical signature of helicene compounds and consists mainly of two peaks, one at 427 nm, the most intense, and one at 450 nm. The solid-state emission shows a bathochromic shift of the two peaks of 7 nm and 5 nm, respectively, with the same relative intensity and a broad band appearing around 550 to 650 nm. This band is attributed to the formation of an excimer between the pyrene moieties at positions 2 and 15 of the helicene, as can be seen by plotting the difference between emissions of enantiomeric **Hel-Si$_n$** in the solid state and monomeric **Hel-Si$_n$** in solution. In contrast, no excimer was observed in dilute solution (10^{-5} M). This lack of visible excimer formation in the monomer indicates that excimer formation in the solid state likely involves two pyrene moieties from different molecular points, supporting the intermolecular nature of the excimer.

Consequences in the CPL activity of Hel-Si$_n$ in solution and in the solid state

The chiroptical properties of helicenes prompted us to investigate the consequences of the excimer state on the CPL activity of **Hel-Si$_n$**. Fig. 6 shows the solution CPL spectra of the three enantiomer pairs of the **Hel-Si$_n$** molecules, which generally have the same shapes and CPL dissymmetry factors (g_{lum} values) on the order of $\pm 7 \times 10^{-3}$. Interestingly, these values are similar in both magnitude and sign to the g_{abs} at lower energy (of positive sign for the *P* enantiomers, see Table 2), suggesting that the same excited state is involved upon excitation and emission, with very low electronic and geometric reorganization. We rationalize that this similarity originates from a behaviour closely related to that of the classical helicene derivatives in the solution.[1]

The situation is different for the ordered nanostructures in bulk where higher g_{lum} values were observed (up to 5 times higher, see Table 2 and Fig. 6). Furthermore, while the CPL bands for **Hel-Si$_7$** and **Hel-Si$_{11}$** are centred at monomer emission wavelengths similar to those in the solution state, this is not the case for **Hel-Si$_3$**. In fact, **Hel-Si$_3$** showed high CPL activity around 550 nm, *i.e.* in the excimer emission region,

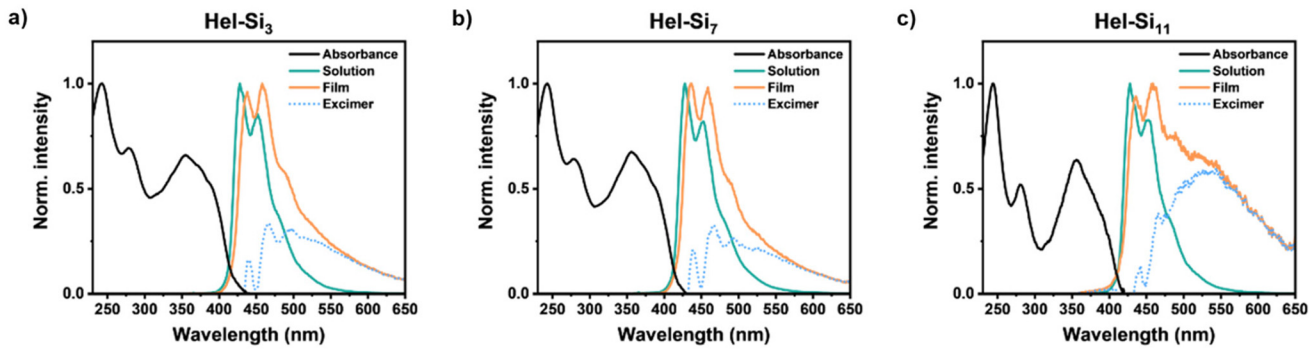

Fig. 5 Absorption and emission spectra of *M*-**Hel-Si$_n$** (a, b, and c for n = 3, 7 and 11, respectively) in 10^{-5} M THF solution and in the solid state recorded as a thin film. The dotted blue trace is the difference between the emission spectra in the solid state and solution to show the excimer. The spectra have all been normalized to unit intensity. The spectra for *P* enantiomers are similar (Fig. S70†).

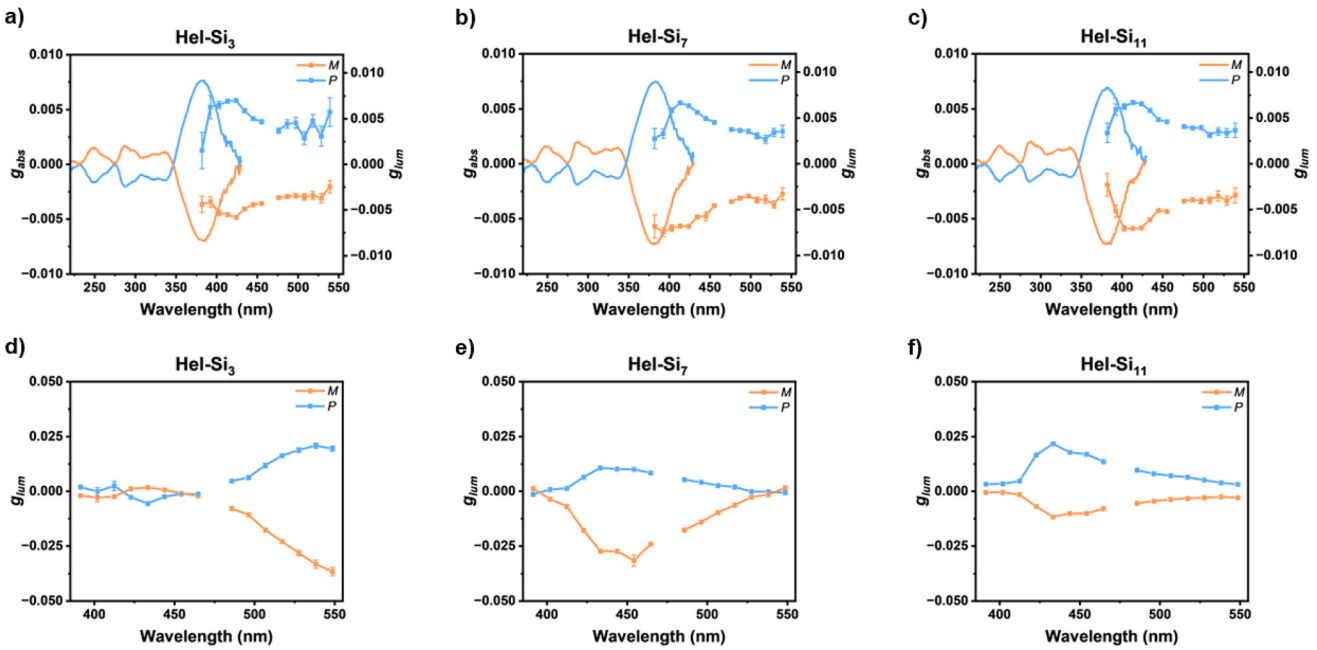

Fig. 6 (a–c) Absorption and emission dissymmetry factors g_{abs} and g_{lum} of **Hel-Si$_n$** in solution (C = 10^{-5} M in THF) and (d–f) emission dissymmetry factors g_{lum} of **Hel-Si$_n$** in the solid state.

Table 2 Absorption and emission dissymmetry factors g_{abs} and g_{lum} found for **Hel-Si$_n$** (a) in 10^{-5} M THF solutions and (b) in the lamellar solid state (see the ESI† for excitation wavelengths)

		M-**Hel-Si$_3$**	*P*-**Hel-Si$_3$**	*M*-**Hel-Si$_7$**	*P*-**Hel-Si$_7$**	*M*-**Hel-Si$_{11}$**	*P*-**Hel-Si$_{11}$**	*P*-**Hel-OMe**	*M*-**Hel-OMe**
Solution (THF)	g_{abs} (λ_{abs})	-7.0×10^{-3} (382 nm)	$+7.6 \times 10^{-3}$ (382 nm)	-7.2×10^{-3} (382 nm)	$+7.4 \times 10^{-3}$ (382 nm)	-7.2×10^{-3} (382 nm)	$+6.8 \times 10^{-3}$ (382 nm)		
	g_{lum} (λ_{lum})	-5.5×10^{-3} (422 nm) ± 1.3×10^{-4}	$+6.9 \times 10^{-3}$ (422 nm) ± 2.3×10^{-4}	-6.8×10^{-3} (422 nm) ± 1.0×10^{-4}	$+6.3 \times 10^{-3}$ (422 nm) ± 1.2×10^{-4}	-7.0×10^{-3} (422 nm) ± 1.1×10^{-4}	$+6.7 \times 10^{-3}$ (422 nm) ± 1.3×10^{-4}	-5×10^{-3} (440 nm)	$+6 \times 10^{-3}$ (440 nm)
	Φ_{lum} (%)	13.4[a]		12.3[a]		13.2[a]		10[b]	
Lamellar solid state	g_{lum} (λ_{lum})	-1.9×10^{-2} (538 nm) ± 1.9×10^{-3}	$+3.6 \times 10^{-2}$ (538 nm) ± 1.1×10^{-3}	-2.7×10^{-2} (440 nm) ± 2.2×10^{-4}	1.0×10^{-2} (440 nm) ± 2.6×10^{-4}	-1.2×10^{-2} (433 nm) ± 3.0×10^{-4}	2.1×10^{-2} (433 nm) ± 2.7×10^{-4}		
	X-fold increase[c]	3.4	5.2	3.9	1.6	1.7	3.1		
	Φ_{lum} (%)	5.9[a]		6.6[a]		8.1[a]			

[a] Measured for the racemic form (see Table S4†). [b] Measured for the racemic form in CH_2Cl_2 (see Table S5†). [c] Calculated ratio of g_{lum} values between the lamellar solid state and the solution.

but showed almost no signal in the monomer emission region, indicating intermolecular interactions between pyrenes in a chiral arrangement. In contrast, as the length of the siloxane chain is increased, the lamellar packing prevents the chiral intermolecular arrangement of pyrenes for CPL emission of excimers. This nicely illustrates how the solid-state supramolecular organization affects the overall chiroptical properties when going from **Hel-Si$_3$**, which exhibits excimer of chiral nature, to **Hel-Si$_7$** and **Hel-Si$_{11}$**, which show chiroptical properties similar to the monomer. It seems that the disordered nature of **Hel-Si$_3$** gives more degrees of freedom to the system, enabling it to achieve chiral excimeric nature through the pyrene units.

Conclusion

We have presented the assembly and chiroptical properties of oligodimethylsiloxane-helicene with varying lengths of discrete siloxane oligomers in solution and bulk. In apolar and polar solutions, these BCOs do not aggregate and exhibit the same chiroptical response as the helical backbone without the *o*DMS units. Different properties were found between the racemic and enantiopure systems. In bulk, pure enantiomers of **Hel-Si$_n$** with short *o*DMS chains (3 repeating units) form a disordered phase, while with longer *o*DMS chains (7 and 11 repeating units), they assemble into an ordered 2D lamellar morphology. As a result of these different assembled structures, different chir-

optical properties are obtained. While the less-ordered state of **Hel-Si$_3$** exhibits CPL emission from an excimer of chiral nature, the lamellar structures of **Hel-Si$_7$** and **Hel-Si$_{11}$** show CPL emission from the monomer but hardly any circular polarization in the emission of the excimer. Overall, up to a 5-fold increase in CPL was observed in the solid state as compared to the solution, with a clear influence of the pyrene excimer emission. These results demonstrate that control of the bulk assembly by molecular design allows for the modulation of chiroptical emission. The transition from single molecules in solution to functional supramolecular structures in soft matter is enabled by the functionalization of helicenes with discrete *o*DMS chains. Hereby, a step forward is made in the construction of bulk supramolecular systems with tuneable chiroptical properties.[13]

Author contributions

S. Cadeddu: synthesis and spectroscopic characterization; B. W. L. van den Bersselaar: POM, DSC, and MAXS/WAXS measurements; Bas de Waal: synthesis of discrete *o*DMS; S. Cadeddu and B. W. L. van den Bersselaar: data curation, formal analysis, visualization, and writing; S. Meskers: chiroptical and emissive properties and writing; N. Vanthuyne: isolation of enantiomers; M. Cordier: X-ray analysis; G. Vantomme and J. Crassous: conceptualization, supervision, validation, writing – review & editing and funding.

Data availability

The data supporting this article have been included as part of the ESI.†

Conflicts of interest

There are no conflicts to declare.

Acknowledgements

We acknowledge the Ministère de l'Education Nationale, de la Recherche et de la Technologie, the Centre National de la Recherche Scientifique (CNRS). The European Commission Research Executive Agency (Grant Agreement number: 859752 – HEL4CHIROLED – H2020-MSCA-ITN-2019), the Dutch Research Council (OCENW.M20.256), and the Dutch Ministry of Education, Culture and Science (Gravity program 024.005.020) are thanked for financial support. Prof. E. W. Meijer is warmly thanked for insightful discussions.

References

1 (*a*) Y. Shen and C.-F. Chen, *Chem. Rev.*, 2012, **112**, 1463–1535; (*b*) M. Gingras, G. Felix and R. Peresutti, *Chem. Soc. Rev.*, 2013, **42**, 1007–1050; (*c*) M. Gingras, *Chem. Soc. Rev.*, 2013, **42**, 968–1006; (*d*) C.-F. Chen and Y. Shen, *Helicene Chemistry: From Synthesis to Applications*, Springer, Berlin, Heidelberg, 2017; (*e*) K. Dhbaibi, L. Favereau and J. Crassous, *Chem. Rev.*, 2019, **119**, 8846–8953; (*f*) *Helicenes – Synthesis, Properties and Applications*, ed. J. Crassous, I. G. Stará and I. Starý, Wiley, 2022.

2 (*a*) A. J. Lovinger, C. Nuckolls and T. J. Katz, *J. Am. Chem. Soc.*, 1998, **120**, 264–268; (*b*) K. E. S. Phillips, T. J. Katz, S. Jockusch, A. J. Lovinger and N. J. Turro, *J. Am. Chem. Soc.*, 2001, **123**, 11899–11907; (*c*) T. Kaseyama, S. Furumi, X. Zhang, K. Tanaka and M. Takeuchi, *Angew. Chem., Int. Ed.*, 2011, **50**, 3684–3687; (*d*) T. Hirose, N. Ito, H. Kubo, T. Sato and K. Matsuda, *J. Mater. Chem. C*, 2016, **4**, 2811–2819; (*e*) J. S. Valera, R. Gómez and L. Sánchez, *Org. Lett.*, 2018, **20**, 2020–2023; (*f*) R. Rodríguez, C. Naranjo, A. Kumar, P. Matozzo, T.-K. Das, Q. Zhu, N. Vanthuyne, R. Gómez, R. Naaman, L. Sánchez and J. Crassous, *J. Am. Chem. Soc.*, 2022, **144**, 7709–7719; (*g*) R. Rodríguez, C. Naranjo, A. Kumar, K. Dhbaibi, P. Matozzo, F. Camerel, N. Vanthuyne, R. Gómez, R. Naaman, L. Sánchez and J. Crassous, *Chem. – Eur. J.*, 2023, **29**, e202302254; (*h*) N. Saito and M. Yamaguchi, *Molecules*, 2018, **23**, 277.

3 F. Wang, F. Gan, C. Shen and H. Qiu, *J. Am. Chem. Soc.*, 2020, **142**, 16167–16172.

4 (*a*) B. Oschmann, J. Lawrence, M. W. Schulze, J. M. Ren, A. Anastasaki, Y. Luo, M. D. Nothling, C. W. Pester, K. T. Delaney, L. A. Connal, A. J. McGrath, P. G. Clark, C. M. Bates and C. J. Hawker, *ACS Macro Lett.*, 2017, **6**, 668–673; (*b*) W. Zhang, W. Yang, H. Pan, X. Lyu, A. Xiao, D. Liu, Y. Liu, Z. Shen, H. Yang and X.-H. Fan, *Soft Matter*, 2022, **18**, 3430–3436; (*c*) T. Nishimura, S. Katsuhara, C. Lee, B. J. Ree, R. Borsali, T. Yamamoto, K. Tajima, T. Satoh and T. Isono, *Nanomaterials*, 2022, **12**, 1653.

5 (*a*) R. H. Zha, G. Vantomme, J. A. Berrocal, R. Gosens, B. de Waal, S. Meskers and E. W. Meijer, *Adv. Funct. Mater.*, 2018, **28**, 1703952; (*b*) B. A. G. Lamers, R. Graf, B. F. M. De Waal, G. Vantomme, A. R. A. Palmans and E. W. Meijer, *J. Am. Chem. Soc.*, 2019, **141**, 15456–15463; (*c*) W. Yang, W. Zhang, L. Luo, X. Lyu, A. Xiao, Z. Shen and X.-H. Fan, *Chem. Commun.*, 2020, **56**, 10341–10344; (*d*) M. H. C. van Son, A. M. Berghuis, F. Eisenreich, B. de Waal, G. Vantomme, J. Gómez Rivas and E. W. Meijer, *Adv. Mater.*, 2020, 2004775.

6 A. Terfort, H. Gorls and H. Brunner, *Synthesis*, 1997, 79–86.

7 (*a*) M. Jakubec, T. Beranek, P. Jakubik, J. Sykora, J. Zadny, V. Cirkva and J. Storch, *J. Org. Chem.*, 2018, **83**, 3607–3616; (*b*) F. B. Mallory and C. W. Mallory, *Organic Reactions*, J. Wiley &, Sons, Inc., 1984, vol. 30, pp. 3.

8 J. Wade, F. Salerno, R. C. Kilbride, D. K. Kim, J. A. Schmidt, J. A. Smith, L. M. LeBlanc, E. H. Wolpert, A. A. Adeleke, E. R. Johnson, J. Nelson, T. Mori, K. E. Jelfs, S. Heutz and M. J. Fuchter, *Nat. Chem.*, 2022, **14**, 1383–1389.

9 J. Jacques, A. Collet and S. H. Wilen, *Enantiomers, Racemates and Resolutions*, John Wiley & Sons, 1981.

10 (*a*) B. A. G. Lamers, B. van Genabeek, J. Hennissen, B. F. M. de Waal, A. R. A. Palmans and E. W. Meijer, *Macromolecules*, 2019, **52**, 1200–1209; (*b*) B. A. G. Lamers,

A. Herdlitschka, T. Schnitzer, M. F. J. Mabesoone, S. M. C. Schoenmakers, B. F. M. de Waal, A. R. A. Palmans, H. Wennemers and E. W. Meijer.

11 (*a*) F. Pop, P. Auban-Senzier, A. Frąckowiak, K. Ptaszyński, I. Olejniczak, J. D. Wallis, E. Canadell and N. Avarvari, *J. Am. Chem. Soc.*, 2013, **135**, 17176–17186; (*b*) F. Pop, N. Zigon and N. Avarvari, *Chem. Rev.*, 2019, **119**, 8435–8478; (*c*) B. Rice, L. M. LeBlanc, A. Otero-de-la-Roza, M. J. Fuchter, E. R. Johnson, J. Nelson and K. E. Jelfs, *Nanoscale*, 2018, **10**, 1865–1876; (*d*) L. Favereau, C. Quinton, C. Poriel, T. Roisnel, D. Jacquemin and J. Crassous, *J. Phys. Chem. Lett.*, 2020, **11**, 6426–6434.

12 Y. Nakai, T. Mori and Y. Inoue, *J. Phys. Chem. A*, 2012, **116**, 7372–7385.

13 J. L. Greenfield, J. Wade, J. R. Brandt, X. Shi, T. J. Penfold and M. J. Fuchter, *Chem. Sci.*, 2021, **12**, 8589–8602.